WATER ELECTROLYSIS PROPULSION IN CUBESATS: A CASE STUDY

ESTORIL, PORTUGAL | 09 – 13 MAY 2022

Sascha Dengler [(1)], Felix Ebert [(2)], Chiara Manfletti [(3)], Sebastian Leichtfuß [(4)]

(1) Technical University of Munich, Munich, Germany, Email: sascha.dengler@tum.de
(2) Technical University of Munich, Munich, Germany, Email: felix.ebert@tum.de
(3) Technical University of Munich, Munich, Germany, Email: chiara.manfletti@tum.de
(4) Technical University of Darmstadt, Darmstadt, Germany, Email: leichtfuss@glr.tu-darmstadt.de

KEYWORDS: CubeSat Propulsion, Water Electrolysis, Green Propellants, Debris Mitigation, Attitude control

ABSTRACT:

The application of Water Electrolysis Propulsion to a 3U CubeSat as a de-orbiting kit with attitude control capabilities is evaluated and presented.
Liquid water is decomposed into gaseous hydrogen and oxygen by an electrolysis unit supplied by solar power. A parametrised simulation model of the propulsion system is derived and coupled with a subsequent optimisation to determine operational and design parameters. A blowdown architecture operating at initial pressures of $15bar$ at a nominal thrust of $0.5N$ is derived as being the most mass efficient. A continuous electrolyser power supply of $2W$ and ca. 400 burn cycles lasting $2.5s$ each are required to achieve the prescribed mission requirements.

1. TECHNOLOGY AND REFERENCE MISSION

Using water as a propellant for in-space propulsion systems brings advantages compared to other propellants in use, such as cost reductions due to easy handling and availability as well as high performance in terms of its energy density. If decomposed into hydrogen and oxygen, it also brings a high specific impulse (I_{sp}) as a result of the propellant combination. In the case of Water Electrolysis Propulsion (WEP), this decomposition is achieved by using an electrolysis unit, fuelled by solar power.
In recent years, the interest in application of such technologies is on the rise, in part due to EU's REACH regulation, which may ban hydrazine and propellants alike.
In addition to combustion in the propulsion unit, the hydrogen and oxygen produced can also be used to supply life support systems or to act as energy source through backwards conversion using a fuel cell. Mining water on celestial bodies and subsequent fuelling operations are also well within the future scope of water propulsion.
These promising advantages however come at the cost of system complexity and mass added by the electrolysis process. Finding ways and solutions to keep complexity low and optimising the systemic design with respect to its mass are key factors to enable broader application of the technology.

1.1 Water Electrolysis Propulsion

The WEP technology centres around taking water as an inert fluid into orbit and subsequently producing combustible propellants on demand via electrical power. This qualifies the system as a 'hybrid', with specifications and characteristics in between pure chemical and electrical propulsion systems.

Once the propellants in form of gaseous oxygen and hydrogen are produced, they can fuel different modes of propulsion. This includes chemical hot and cold gas thrusters and possibly electrical propulsion systems. A schematic overview of the WEP system with a cold gas thruster array is depicted in Fig. 1. Pressurisation of the gases is realised by the electrolysis process itself and does not require additional active components such as pumps.

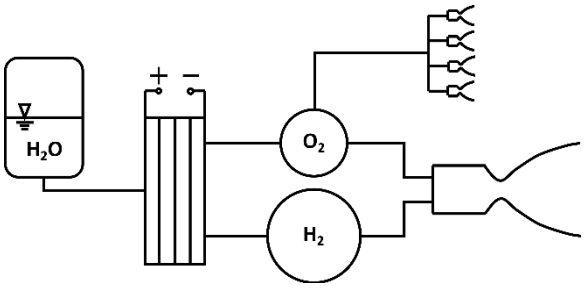

Figure 1: Schematic of a Water Electrolysis Propulsion System.

In the scope of this work, a chemical propulsion setup is considered, consisting of a hot gas thruster as delta-v motor and an additional cold gas thruster array for satisfying attitude control requirements.

1.2 CubeSat Platform

The CubeSat platform is an attractive application case for WEP not only motivated by being a cost-efficient way to demonstrate newly developed technologies in space, but also because of the existing commercial market itself. The amount of

CubeSats launched is continuously on the rise at an ever-increasing rate [1], which comes with a growing demand for flexible, performant and affordable propulsion systems.
CubeSats are configured in increments of so-called units, whereby one Unit (1U) describes a cube with $10cm$ edge length and a maximum mass of $2kg$ [2]. These satellites are frequently built using components off the shelf (COTS), which makes them more affordable compared to custom satellite systems tailored to a specific application.
A first demonstration mission verifying the feasibility of the WEP technology was recently carried out as part of NASA's PTD-1 mission on a 6U CubeSat in 2021 [3].

1.3 Reference Mission

When looking at the current distribution of configurations and orbits of CubeSat missions, the most common setup is a 3U platform operating with an earth observation objective at polar orbits of around $500km$ altitude [4]. This configuration is therefore chosen as reference for the subsequent design considerations in this paper. As reference mission with an emphasis on space debris mitigation, an active de-orbit manoeuvre after end of mission life is modelled. This involves decreasing the perigee to $200km$ from an initial $500km$ circular sun-synchronous orbit (SSO) to then passively de-orbit in less than one month due to atmospheric drag. The key specifications and requirements for this mission are summarised in Tab. 1.

Table 1: Summarised Reference Mission Parameters.

Parameter	Value	Unit
Δv	85	m/s
Overall Impulse	500	Ns
Initial perigee altitude	500	Km
Final perigee altitude	200	Km

Besides the de-orbit manoeuvre, an additional requirement to provide attitude control is set. This is to fulfil mission pointing needs as well as to compensate for disturbing torques, which can be caused by thrust vector misalignments of the hot gas thruster.
The attitude control demand has an impact on propellant allocation between the two propulsion subsystems and will be further discussed in section 2.3.
Furthermore, when factoring in the current market situation, the propulsion submodule should be contained within 1U to allow for modular integration of the satellite and sufficient volume for bus and payload.

2. DESIGN CONSIDERATIONS

For further assessment and to meet the reference mission objectives set, preliminary design considerations and subsequent decisions are presented in this chapter. This includes the electrolyser, the propellant feed options and interactions between the main thruster and attitude control system.

2.1 Electrolysis

The main constraint the electrolysis unit poses on the overall system is a limited propellant production rate given by the available electrical power supply from solar arrays. Power supply and production rate are interconnected due to the energy needed to decompose the H_2O molecule into O_2 and H_2. The energy required is equivalent to the calorific value of the produced hydrogen (higher heating value, 286 kJ/mol) [5]. This corresponds to an attainable mass flow rate of propellants (H_2 + O_2) that is dependent on the supplied power (Eq. 1).

$$\frac{\dot{m}}{P} = 0.775\, x10^{-7}\, Kgs^{-1}W^{-1} \qquad \text{Eq. 1}$$

However, an electrolysis unit does not operate loss-free, and the efficiency of the unit is strongly dependent on operational parameters such as backpressure of the produced gaseous propellants and temperature of the unit. Typical efficiencies are found to be in the range of $67 - 82\ \%$ [5].
Regarding solar power, a side panel of a CubeSat ($10cm$ x $10cm$) covered by solar arrays can provide a continuous power supply of max. $2.3W$. To avoid additional complexity, mass and costs, deployable solar array mechanisms should be avoided. Since the WEP unit shall not exceed 1U of volume, the average surface area exposed to sunlight corresponds to one of such panels. That confines the achievable production mass flow rate to an order of magnitude of $10^{-4}\ g/s$ at an assumed continuous power supply of $2W$.
For the electrolyser to work in a microgravity environment, special consideration needs to be given to the design of its architecture and adjacent components. A Proton exchange membrane (PEM) setup is a suitable technology to satisfy this requirement [6].
It should be noted that decomposing H_2O yields the products H_2 and O_2 in the stoichiometric mass ratio of 8. Furthermore, the gases produced consist of impurities such as remaining humidity or cross-contamination of the products to some extent.

2.2 Feed System Architectures

The representative mass flow rate derived in the previous chapter makes direct, continuous propellant feed from the electrolyser and continuous combustion in the hot gas thruster difficult to achieve. There is poor availability of commercial components in this order of magnitude, while additional phenomena need to be considered such as rarefaction and boundary layer influence. Those significantly increase the uncertainties in the design

process and potentially reduce overall efficiency. Thus, in this case study, intermediate storage of the gaseous propellants is necessary. Gas run tanks are therefore required as depicted in Fig. 2. The configuration of components downstream of the run tanks resemble a typical chemical propulsion system. When looking at configurations to feed the propellants to the hot gas thruster, two options are possible:

(1) Quasi steady feed with pressure regulators upstream of the main valves (right side in Fig. 2).
(2) Blowdown, transient feed with no pressure regulators present (left side in Fig. 2).

Venturis are implemented in both versions to set a nominal mass flow rate towards the thruster.
While (1) allows operation of the thruster at its design point and therefore presumably comes with higher efficiency in terms of I_{sp}, the added mass and complexity of the additional components must be considered.

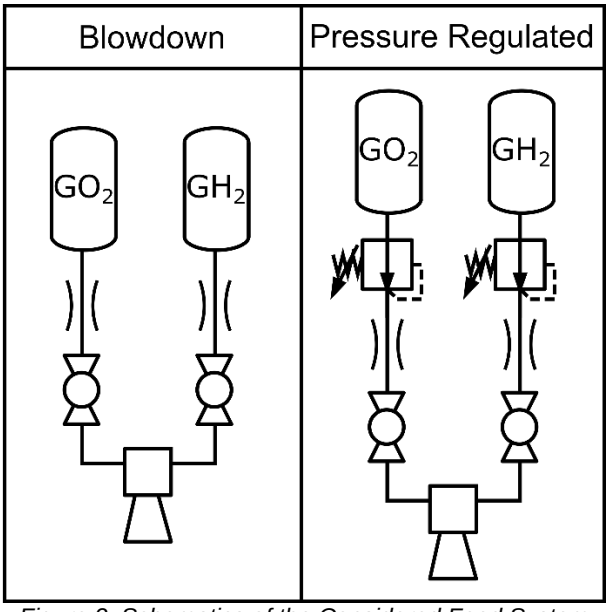

Figure 2: Schematics of the Considered Feed System Architectures.

Associated to this trade-off, questions regarding an optimal operation and design point arise. The parameters that determine the design point are nominal pressures, mass flows and oxidiser-fuel-ratio (OF). The trade-offs between these variables need a quantitative assessment of the implications of their variation on performance and other metrics. The simulation and optimisation performed to this end are described in the subsequent chapters.

2.3 Oxidizer Fuel mixture ratio

There are two main factors strongly influencing the choice of the OF for the main thruster: Dependency of the thruster mixture ratio on the expected I_{sp} as well as propellant demand of the attitude control system (ACS). The first is quantified by approximating the exhaust velocity using the Bernoulli equation for isentropic, compressible flows and rearranging with respect to the outflow velocity v_e (see Eq. 2):

$$v_e = \sqrt{\frac{2\gamma}{\gamma-1}\frac{RT_c}{M}\left[1-\left(\frac{p_e}{p_c}\right)^{\frac{\gamma-1}{\gamma}}\right]} \qquad \text{Eq. 2}$$

To obtain the combustion temperature T_c, chemical equilibrium is assumed. The reaction is assumed to remain 'frozen' when leaving the combustion chamber and entering the convergent nozzle part, thus no shift in chemical equilibrium composition is considered. Furthermore, the combustion is assumed to be adiabatic, meaning no heat transfer to the walls is present. Evaluating this function for different OF's at an arbitrary combustion pressure of $5bar$ and when expanding into vacuum yields the curves shown in Fig. 3.

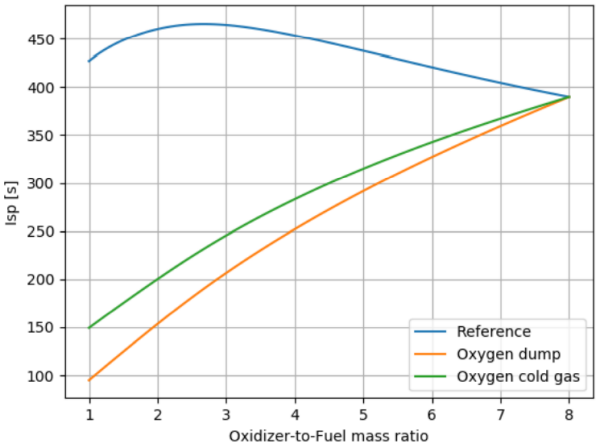

Figure 3: I_{sp} depending on OF and Operation Strategy.

A decrease in OF from its stochiometric value of 8 improves the I_{sp} (blue curve), since the influence of the lower molar mass in more fuel rich mixtures outweighs the reduced combustion temperature, which is highest at stoichiometry.
However, when considering operating the main thruster at a fuel rich OF, the fact that not all of the propellants produced contribute to the Δv generated by the main thruster must be taken into account. As previously shown by [7], the overall propellant efficiency with respect to the carried water is highest when operating the main thruster at the stoichiometric production ratio. The unused amount of 'dumped' oxygen outweighs the slight I_{sp} increase of fuel rich combustion (orange curve in Fig. 3), resulting in a reduced 'systemic' I_{sp} that factors in the unused oxygen mass. This also remains true if the oxygen would be used in a cold gas configuration to contribute to the Δv generated (green curve in Fig. 3).
At stoichiometric operation, a theoretical maximum I_{sp} of ca. $390s$ is attainable considering the assumptions made.

As previously mentioned, the ACS poses an additional propellant demand. To keep system complexity low and facilitate a low-cost approach, a cold gas system using a single propellant species is favoured.
This leaves the choice of which propellant to use. While there is 8 times as much oxygen available than hydrogen in terms of mass, the performance must also be considered. Using Eq. 2, an approximate specific impulse for cold gas operation of $\sim 75s$ for oxygen and $\sim 300s$ for hydrogen is obtained. Taking both these factors into account, O_2 provides approximately double the overall impulse. Furthermore, since a fuel-rich combustion offers some potential advantages such as higher I_{sp}, lower combustion temperatures and avoidance of high temperature oxidation, O_2 is favoured for the attitude control system. Yet, the propellant consumption of the ACS shall still be minimised to maximise the overall system efficiency in terms of the total amount of water needed, as shown in Fig. 3.

To obtain a first approximation of the propellant demand of the ACS and its implication on the OF of the main thruster, the thrust vector control phase is analysed. During this phase, the highest disturbing torques are expected, which need to be corrected while the main thruster is firing. This requires reserving some amount of the oxygen for the ACS, thus reducing the main thruster OF.
A typical misalignment of the main thruster that can be expected has a magnitude of ~ 2 degrees [8]. The given geometrical specification of the CubeSat with the expected misalignment yields a disturbing torque, that the ACS needs to counteract. Assuming a setup of the cold gas thrusters that achieves a maximal leverage, a momentum balance can be derived. Fig. 4 depicts the simplified geometrical relations of the moment balance.

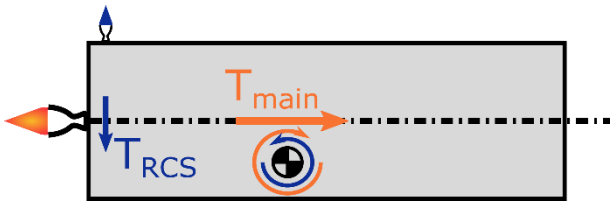

Figure 4: Forces and resulting Torques during Hot Gas Thrust Event and RCS Firing.

The oxygen demand thus becomes a function of the extent of the misalignment, the geometrical properties of the satellite as well as the specific impulse of main thruster and cold gas system.
The momentum balance can be fulfilled with an OF of 7, that allows for enough oxygen reserve for the ACS the counteract the given thrust vector misalignment.

2.4 Thermal considerations

The derived, close-to-stoichiometric propellant ratio of 7 entails high combustion temperatures exceeding $3000K$.
This, in combination with the absence of cryogenic cooling fluids as would be the case in many common rocket engines, does require special attention to the thermal management of the thruster.
In order to be cost-effective, a passive solution making use of the heat sink capabilities of the wall material itself is favoured at this point. A capacitive cooling approach inherently means that achievable burn times of the thruster are limited, as the melting point of most materials lie well below the combustion temperatures. Any measures to locally reduce the heat influx to the wall may be considered in the future, e.g. stratified combustion as in ArianeGroup's DM1 thruster [6].
Another restraint that limits the burn time is the amount of stored gaseous propellants as these are only intermediately stored. A large storage capacity would lead to heavy tanks and thus increase system dry mass.
A preliminary modelling of the heat transfer behaviour with 1D simplifications shows that feasible burn times are in the order of a few seconds. The attainable burn time is dependent on the hot gas properties but also on the properties of the thruster material.
Due to the limited burn time and the entailed non-stationary operating conditions, transient effects become of increased importance. A transient simulation approach is required to further access the quantitative behaviour of discussed considerations on system components.

3. SIMULATION SETUP

A transient simulation of the chemical propulsion system in different configurations is implemented. The implemented models are parameterised to allow for a subsequent optimisation of design and operational variables.
The simulation is carried out using the software EcosimPro in combination with the European Space Propulsion System Simulation (ESPSS) toolkit, which contains libraries with pre-defined space propulsion components. The simulation itself makes use of 1D gas dynamics simulation as well as chemical equilibrium assumption for combustion.
A special focus is set on the chemical propulsion part of the WEP system. Thus, the system is modelled downstream of the electrolyser, including the gas run tanks. The parametrisation is conducted with respect to several system variables of interest. The parameters incorporated are the following:

- Nominal combustion pressure
- Nominal propellant mass flow
- Initial storage pressure in gas run tanks
- Cut-off pressure in gas run tanks
- Propellant mixture ratio (OF)
- Expansion ratio of the nozzle

3.1 Topology and Component Sizing

The topology of the implemented simulation models is similar to the schematics shown in Fig. 2, making use of the components provided by the ESPSS libraries. Complementary to the topology used, the properties, conditions and geometrical parameters of components and the fluids of the system are modelled by using the mentioned parameters as input variables.
The components of the feeding system upstream of the thrust chamber are characterised using assumptions of isentropic, compressible flow to determine throat diameters of the venturis as well as the pressure regulators.
The throat diameter of the thruster is also derived from the compressible Bernoulli equation assuming isentropic conditions. The combustion chamber sizing is based on the Humble correlation [9] with the chamber volume being calculated with an assumed characteristic length of $0.6m$. The injection is set to induce a pressure-loss of 20% of the nominal combustion pressure.
Ignition is initiated by setting a flag at a certain timestamp, from which reaction and combustion of the propellants take place instantaneously. To obtain a feasible delay time from injection to actual ignition and thus the mentioned timestamp, a closer look at possible ignition methods must be taken. Resonance ignition is determined to be a suitable technology due to its passive setup and good compatibility to the propellants used. This method makes use of an oscillating shock structure of a supersonic stream injected into a cavity, which is designed such that resonance occurs. Literature suggests a typical ignition delay time for resonance ignition of $0.2s$ [10], which is implemented as timestamp in the simulation model.

Concerning the gas run tanks, mass and volume are the main factors of interest. Since the available volume is constricted due to the requirement of being confined to 1U, the maximum realisable volume for the gas tanks is fixed at $100ml$. This particular volume emerges from packaging considerations and the space being taken up by the electrolyser, the water tank, the main and cold gas thrusters.
The actual storage capacity is thus driven by the pressure of the gases. Dry mass of the tanks is determined using Barlow's law with volume, pressure, safety factor and material properties as input parameters. The tanks are assumed to be made of aluminium at a safety factor of 2.

3.2 Thermal Setup

The thruster wall experiences heat fluxes due to convection and radiation at the inner thruster wall, facing the hot gases. On the outside, the only mechanism to be considered in space is radiation. This heat flux is however neglected in the thermal setup in Ecosim, as it has been shown during the analysis that the radiation influence on the outside is negligible over the course of a short duration thrust event.
The convective heat flux is proportional to the heat transfer coefficient h_g and the temperature difference between hot gases and thruster wall $\Delta T = T_{hotgas} - T_{wall}$. The heat transfer coefficient is calculated according to the Bartz equation (see Eq. 3).

$$h_g = \frac{0.026}{d_{th}^{0.2}} \cdot \left(\frac{\eta^{0.2} c_p}{Pr^{0.6}}\right) \cdot \left(\frac{p_c^*}{c^*}\right)^{0.8} \left(\frac{A_{th}}{A}\right)^{0.9} \sigma \qquad \text{Eq. 3}$$

As can be seen from Eq. 3, the heat transfer coefficient and thus the convective heat flux depends on the local diameter of the stream channel. To account for the variations along the chamber axis, the chamber is discretised in axial direction.
The only molecule considered for radiation in the EcosimPro setup is water. Eq. 4 shows the dependency of the radiative heat flux on the partial pressure p_{H_2O} of the water vapor [11].

$$\dot{q}_{H_2O} = 4.07 \cdot \left(\frac{p_{H_2O}}{98066.5}\right)^{0.8} \cdot L^{0.6} \cdot \left(\left(\frac{T}{100}\right)^3 - \left(\frac{T_{wall}}{100}\right)^3\right) \qquad \text{Eq. 4}$$

In the simulation model developed, the thrust chamber wall is geometrically approximated as a flat plate. This is a simplification in contrast to the real geometry since the curvature of the combustion chamber wall is not considered. This directly affects the temperature development, which is discussed further in chapter 6.2.
In addition to the geometry, the material properties of the chamber wall affect the temperature evolution of the thruster. For the sake of this case study, Inconel 718 is chosen as thruster material. This is due to the suitable compromise between good availability and cost as well as favourable temperature resistance and mechanical properties. An additional benefit of Inconel is the melting point being still low enough such that it burns up when re-entering earth's atmosphere, thus reducing the risk of debris impact on the ground. A discussion on material choice is given in chapter 5.2.

4. CHARACTERISTIC BEHAVIOUR

The results of the simulation for arbitrary sets of input variables already yields a basic understanding of the qualitative behaviour of the chemical propulsion subsystem.
Due to the modelling approach in ignition delay behaviour, a distinct pre-ignition phase is observed when looking e.g. at the pressure evolution (Fig. 5).

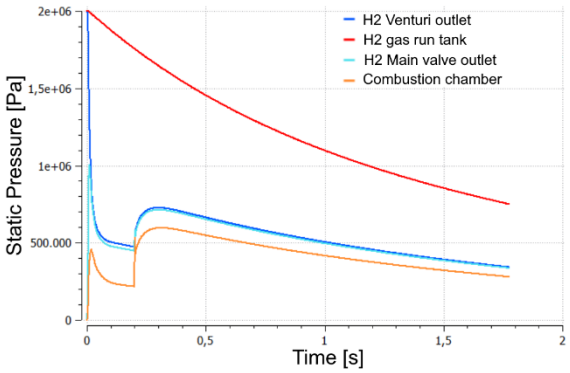

Figure 5: Simulated Pressure evolution over Time of the blow-down variant.

Due to the lack of combustion back-pressure prior to ignition, the mass flow rates are temporarily significantly higher than the nominal design point suggests. The mass flow rate is determined by the upstream pressure and the smallest cross-sectional area where the flow is choked. While the latter remains geometrically fixed in a flow venturi, the upstream pressure is at its highest in the pre-ignition phase. Due to the propellants leaving the chamber without being combusted in the pre-ignition phase, this is a loss-mechanism since the calorific value remains unused.
This characteristic behaviour is more amplified in the blowdown variant of the system, due to the venturis experiencing the full upstream storage pressure.

A typical temperature evolution of the combustion chamber wall is shown in Fig. 6. The heat flux is calculated according to the Bartz correlation, which is defined in Eq. 3 [12].

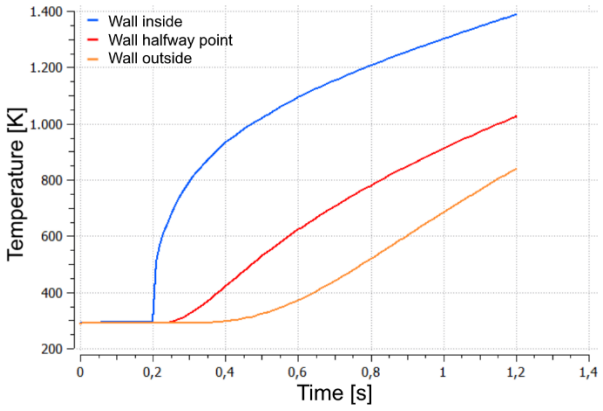

Figure 6: Simulated wall temperature evolution at different radial locations at the throat.

In the initial time after ignition, heat flux is at its maximum. This is due to the temperature gradient between hot gas and wall being at its highest. Furthermore, combustion pressure contributes almost linearly to the heat flux, as the Bartz correlation suggests. For the blow-down variant, the combustion pressure is at its highest shortly after ignition. What can be seen as well, for this arbitrary combination of parameters, is that the inner wall temperature at the throat almost reaches the melting point just after $1s$ of burn time. This corresponds to the findings in the previous chapter and underlines again the importance of thermal management of the thruster. The heat flux entering the thruster material is energy lost for conversion into kinetic energy of the hot gases, thus reducing the achievable I_{sp}.
The resulting averaged I_{sp} over a thrust pulse ranges at around ~$300s$, which is significantly lower than the theoretically possible $390s$ under frozen assumption. Taking a closer look at the loss mechanisms, the previously discussed heat and ignition losses are at the root for the reduced efficiency of the simulated setup. To further quantify this assumption, two loss factors are defined by using the calorific value as a reference.
For quantifying the losses induced by the pre-ignition phase, an ignition loss index L_{ign} is defined by denominating the calorific value of the unburnt propellants by the integrated calorific value of the consumed propellants of the thrust pulse (see Eq. 5).

$$L_{ign} := \frac{\int_0^{t_{ign}} LHV_{H2}\, \dot{m}_{H2}\, dt}{\int_0^{t_{end}} LHV_{H2}\, \dot{m}_{H2}\, dt} \qquad \text{Eq. 5}$$

Furthermore, the heat losses are accounted for via a thermal loss index L_{th}. The index is determined by the integrated heat flux to the thruster being denominated by the calorific value of the consumed propellant (see Eq. 6).

$$L_{th} := \frac{\int_0^{t_{end}} \dot{Q}_{thruster}\, dt}{\int_0^{t_{end}} LHV_{H2}\, \dot{m}_{H2}\, dt} \qquad \text{Eq. 6}$$

These loss indices can be evaluated by continuous integration over the transient thrust pulse, which is depicted in Fig. 7.

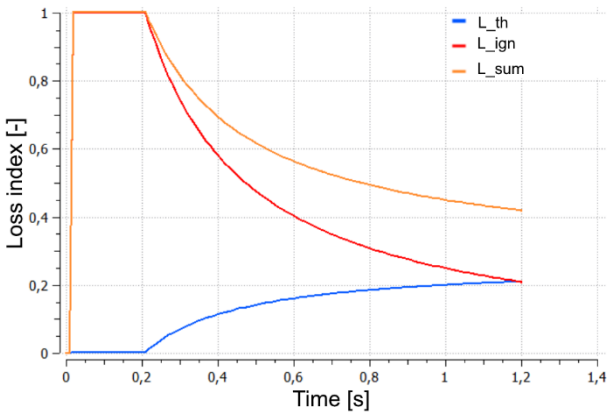

Figure 7: Simulated loss indices over time.

While the loss attributed to unburnt propellants is compensated with longer burn times, the heat loss sharply increases directly after ignition and then shows asymptotic behaviour with additional burn

time, since the thermal conditions approach steady state. In this example, the losses add up to about 40% of the overall provided calorific value of the propellants. As can be seen, the sum of those losses still shows a decreasing tendency towards the end of the thrust pulse, which means I_{sp} can be increased by longer burn durations. However, the maximal temperature of the wall material is limited, which inherently leads to a trade-off when wanting to maximise overall propellant efficiency.

5. OPTIMISATION

To gain insight into the impact of design and operational point variations, an optimisation on basis of the parameterised simulation model presented in the previous chapter is conducted.

The optimisation's main objective is to minimise the overall system mass. This is to include trade-offs on a systemic level such as improved specific impulse vs. heavier tanks when increasing system pressures. For determination of the 'variable' system masses, the components that are being considered are gas run tank dry mass, thruster mass and the required propellant mass to conduct the reference manoeuvre in dependence of the achieved systemic I_{sp}. Remaining components like valves and the like were assumed to be COTS and therefore remain unchanged in their properties when varying the input variables.
Secondary threshold conditions were implemented as well to account for boundaries set by the mission profile, material properties or geometrical considerations. One major constraint is the maximum tolerable wall material temperature that must not be exceeded, otherwise the design is labelled as not feasible.
The optimisation is implemented using Esteco's modeFrontier and making use of the proprietary algorithm pilOPT. An overview of the results is presented in Tab. 2 and Tab. 3. The values regarding the blowdown system are to be interpreted as nominal values of the design point since operation is dominantly transient.

Table 2: Resulting Optimised Design Parameters.

Parameter	Steady	Blowdown
OF [-]	7	7
Combustion Pressure [bar]	1.9	3.5
Storage Pressure [bar]	14.5	14.2
Cut-off Pressure [bar]	3.6	3.5
Propellant Mass Flow [g/s]	0.13	0.21

5.1 Feed architecture

When comparing the steady feed architecture with pressure regulators to the blowdown operation in Tab. 3, the results suggest that the latter is less efficient in terms of specific impulse. This is as expected, since the thruster of fixed geometry is not operated at its design point during blowdown operation, but rather over a range of conditions. However, the magnitude of the actual difference is of interest. The I_{sp} advantage of additional $\sim 16s$ translates to propellant savings of ca. $10g$ for the given Δv requirement. To ensure steady flow conditions in the feed system, additional pressure regulators are necessary. It is questionable whether a mass budget of $10g$ is sufficient to employ two regulators for each the fuel and oxidiser lines. The gained advantage in terms of I_{sp} vanishes, at least for the considered reference mission. For mission profiles with higher Δv demands, the propellant savings due to the increased I_{sp} are more significant and employing pressure regulators for steady operation could potentially be advisable.

Table 3: Properties of the Optimised Systems.

Parameter	Steady	Blowdown
Variable System Mass [g]	251	260
I_{sp} [s]	316	300
Burn Time [s]	2.50	2.65
Mean Thrust [N]	0.55	0.50

5.2 Burn time and thermal considerations

As discussed in previous chapters, thermal management of the thruster plays a significant role in finding an optimal parameter combination. Looking at the relation of calculated system masses over the resulting maximum temperatures occurring in the thruster underline this statement. A typical pareto front distribution of the simulated design points is observed (see Fig. 8). The general relation is inverse - with higher resulting temperatures, the overall system mass decreases. Higher temperatures are, amongst others, caused by longer burn times and/or higher combustion pressures. The heat flux is proportional to the combustion pressure to the power of 0.8 according to Bartz's correlation (Eq. 3). Burn time and combustion chamber pressure do in turn have a positive correlation with I_{sp}, which reduces the required propellant mass and thus leads to lighter system masses.

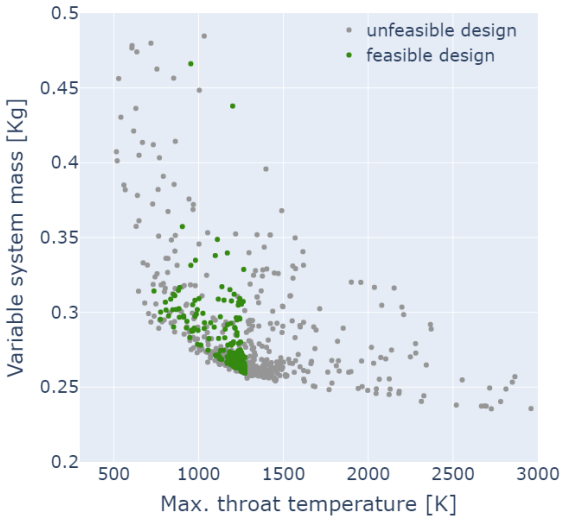

Figure 8: Variable System Mass over Throat Wall Temperature.

The pareto front also gives hints in the direction of favourable materials for such a passively cooled chamber. In case of the investigated setup with Inconel 718 as material, the allowable temperature is set to be $1273K$ which is the threshold for oxidation resistance [13]. However, the higher the allowable temperature is, the better, but with diminishing returns in terms of mass savings. For choosing a suitable material, this then becomes an economic trade-off to be made in terms of performance gained vs. cost. When comparing an Inconel thruster to one made from e.g. Platinum-rhodium, the additional orders of magnitude in material cost might not be worth the improvement in performance for this particular reference mission. However, again for higher Δv mission profiles, the advantage becomes more amplified.

The preliminary analysis of the link between burn time and losses is discussed in chapter 4. Adding to this, the optimisation results yield further insight into the interplay. Looking at the distribution of resulting system mass over the burn time shows a local optimum at just below $3s$ for the feasible design points (Fig. 9). When taking the unfeasible design points into account as well, the previously derived behaviour is confirmed, with the system becoming lighter with longer burn duration due to better fuel efficiency.

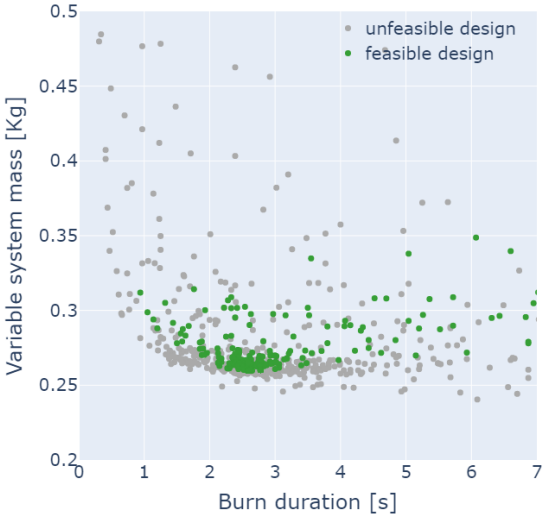

Figure 9: Variable System Mass over Burn Duration.

However, for the feasible design points, an increase in mass with increasing burn time can be observed after the local minimum. This can be traced to the parameter combinations needed to reach such long burn durations without exceeding the critical material temperature. These are very low combustion pressures or low OF that entail a decreased fuel efficiency in terms of systemic I_{sp}. The gradient however remains shallow, indicating that the phenomena are approximately compensating each other. It should also be noted that this means that uncertainties (due to assumptions made and simulation approach used) can shift the actual location of the local minimum significantly.

5.3 Storage and combustion pressure

The initial storage pressure in the gas run tanks is another lever for system performance. Especially in the case of the blowdown architecture, since it determines combustion pressure as well.

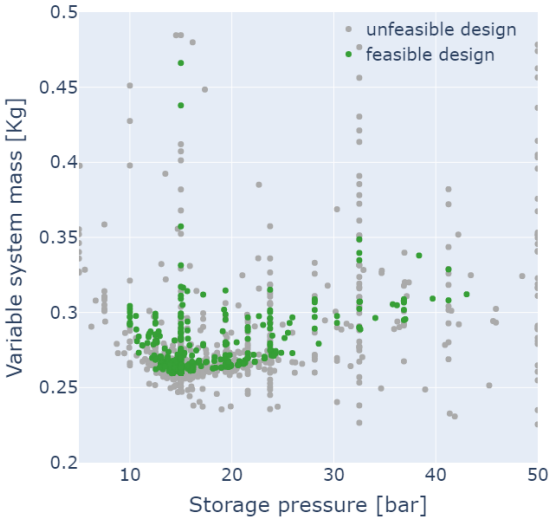

Figure 10: Variable System Mass over Initial Storage Pressure.

In Fig. 10, the system mass as a function of the initial storage pressure is shown. Again, a local optimum can be observed, located at ca. $14bar$. This is the case when considering only feasible design points. Factoring in all evaluated designs, a general tendency towards lower system masses with increasing storage pressures is observed. This indicates that the increased dry mass induced by higher pressures does not outweigh the propellant savings of an increased I_{sp}.
When considering the feasible designs and thus the thermal boundaries of the thruster, this characteristic changes. For higher storage and thus combustion pressures, the burn time must be reduced to remain within the thermal boundaries. As per Eq. 3, the heat transfer coefficient increases with the combustion pressure to the power of 0.8. The imposed shorter burn time takes a toll on I_{sp} and requires more propellant mass to conclude the manoeuvre.
The vertical lines in Fig. 10 are due to the fact that storage pressure is a direct input variable to the simulation and the optimisation algorithm used consists of an initial equidistant variable space exploration.

6. THERMAL ANALYSIS OF THE HOT GAS THRUSTER

In the following, the thermal behaviour of the hot gas engine is investigated in more detail.

6.1 Foundations and Setup

As explained earlier, heat is transferred to the thruster wall by convection and radiation, whereby convection is the dominant mechanism [12]. More precisely, a comparison of the radiative and convective heat flux derived with the analysis tool used for the following study shows that the heat transferred to the thruster wall by radiation does not exceed 0.5% of the heat transferred by convection during the transient thrust event. The driving forces for the convective heat transfer in terms of the heat flux $\dot{q}$ are the heat transfer coefficient h_g and the temperature difference ΔT between thruster wall and the combustion gases, as can be seen from Eq. 7 [14].

$$\dot{q} = h_g \cdot \Delta T = h_g \cdot \left(T_{hotgas} - T_{wall}\right) \qquad \text{Eq. 7}$$

The Bartz correlation is used for the determination of the heat transfer coefficient. However, this correlation is based on turbulent flow [14]. Having Reynolds numbers in the range of $700 - 4300$ in the combustion chamber and throat respectively for the design point conditions, the prediction by Bartz is expected to be conservative. In addition to Bartz, two more correlations are considered for the thermal analysis, namely by Sinyarev (Eq. 8) and by Polifke (Eq. 9-12) [12].

$$h_g = 0.0162 \cdot \left(\frac{\rho u d}{\mu} \cdot Pr\right)^{0.82} \cdot \frac{T_{cc}}{T_{wall}}^{0.35} \cdot \frac{\lambda}{d} \qquad \text{Eq. 8}$$

$$h_g = \frac{\frac{\xi}{8} \cdot (Re - 1000) \cdot Pr}{1 + 12.7 \cdot \sqrt{\frac{\xi}{8}} \cdot (Pr^{\frac{2}{3}} - 1)} \cdot \frac{\lambda}{d} k_\kappa k_{Pr} \qquad \text{Eq. 9}$$

$$\xi = (1.82 \cdot \lg Re - 1.64)^{-2} \qquad \text{Eq. 10}$$

$$k_\kappa = 1 + \left(\frac{d}{l}\right)^{\frac{2}{3}} \qquad \text{Eq. 11}$$

$$k_{Pr} = \left(\frac{\Pr(T = T_{cc})}{\Pr(T = T_{wall})}\right)^{0.11} \qquad \text{Eq. 12}$$

It is expected that the wall temperature evolution predicted by Polifke is the most suitable, since the boundary conditions in terms of Reynolds and Prandtl number are met by the underlying heat transfer problem. The valid Reynolds number range lies between 2300 and 10^6, the Prandtl number range between 0.5 to 500 and the length to diameter ratio fulfils the following criterion: $10 < \frac{l}{d} < \infty$ [12].

However, without experimental validation, it remains uncertain which of the correlations described predicts the occurring heat flux most accurately. This is also due to the scarce literature available on engines in the thrust class of around $1N$. Hence, a test campaign is planned to supplement the simulative approach by experimental data and subsequently compare the prediction accuracy of the different theoretical approaches.

The thermal studies are conducted by means of a transient 1D (radial, circumferential symmetry assumed) heat conduction simulation, with the convective and radiative heat fluxes occurring at the inner thruster wall imposed as transient boundary conditions. The initial wall temperature is $296K$, which corresponds to the equilibrium temperature of the thruster in a SSO entirely exposed to the sun. The thruster material is Inconel 718 with an absorption and emission coefficient of 0.69 [15]. The material properties (heat conductivity, density, specific heat capacity) are interpolated corresponding to the material temperature with values taken from [16] and [17]. As a first approximation, a wall thickness of $3mm$ is used. As the throat experiences the highest heat loads, the analysis focuses on the temperature evolution of the throat [18].

6.2 Sensitivity of Temperature Evolution to Heat Transfer Correlation

The temperature evolutions corresponding to the three different heat transfer coefficient correlations

(Bartz, Sinyarev & Polifke) are shown in Fig. 11.

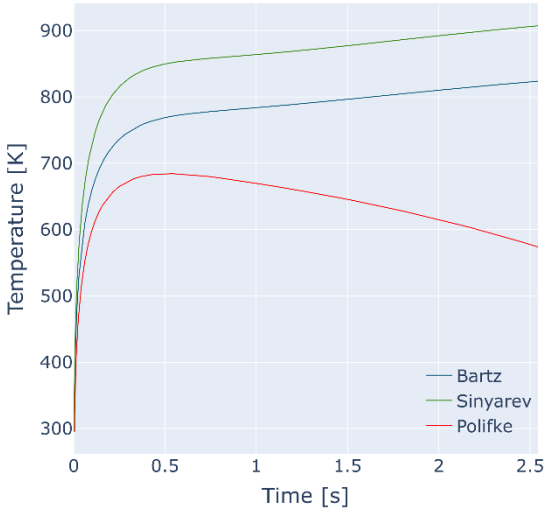

Figure 11: Inner Wall Temperature Evolution depending on Heat Transfer Coefficient correlation.

The temperature gradient within the first $0.15s$ is similar. After the first temperature increase, however, the temperature evolutions differ significantly. While the correlation according to Bartz and Sinyarev are qualitatively similar, Sinyarev predicts a higher maximum temperature at the end of the thrust event than Bartz.
The temperatures stay well below the maximal temperature predicted by the Ecosim model. This is due to the current analysis being conducted considering the curvature of the combustion chamber contour.
By taking curvature into account, each volume element of the mesh that is located further out radially has a greater mass than the previous element. This increases the thermal storage capacity more than linearly in contrast to a flat plate heat transfer problem.
The peak wall temperature for the temperature evolution according to Polifke is reached after $0.5s$, after which the temperature declines although combustion is still going on. This is caused by the fact that the heat transfer coefficient predicted by Polifke is significantly lower than for Bartz ($\approx 75\%$ of Bartz) and Sinyarev ($\approx 60\%$ of Sinyarev), which ultimately results in a negative net heat flow. This means the heat flow entering the combustion chamber wall is lower than the heat conducted radially outwards through the thruster material.

6.3 Wall Thickness determination

Determining the wall thickness is essentially a trade-off between the required cool down time after a thrust event and minimising the heat losses on the one side and preventing thruster fatigue due to wall overheating on the other side.
To quantify the effect of the wall thickness on the temperature evolution, a wall thickness variation of $2.0mm$ to $4.5mm$ in $0.5mm$ steps is conducted and the inner wall temperature evolution at the throat is predicted based on the Sinyarev correlation, since this is the most conservative one.

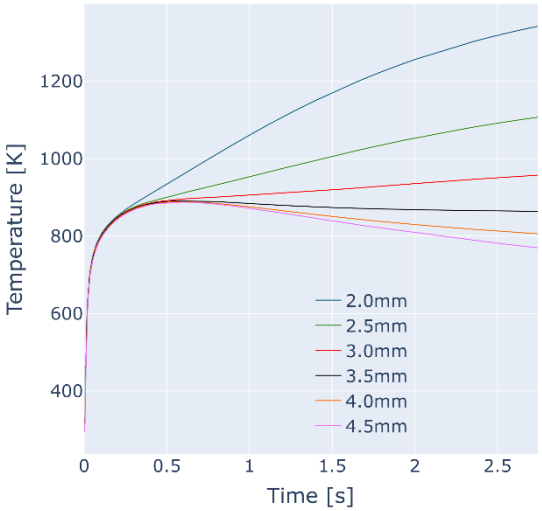

Figure 12: Temperature Evolution for Sinyarev Correlation for different Wall Thicknesses.

Fig. 12 shows the temperature evolution as function sheaf with the wall thickness being the variable parameter. This time, the ignition is expected to occur directly after opening the valves (no ignition delay), which is more conservative, since the heat loads act longer upon the thruster wall, i.e. for $2.7s$ instead of $2.5s$ as before. In contrast to the oxygen resistance temperature limit of $1273K$ described earlier, the thruster manufacturer recommends keeping the temperature below $973K$. Thus, a minimum wall thickness of $3mm$ is required to prevent the material from fatigue due to overheating.

As mentioned previously, the cooling period of the thruster material in between thrust events depends on the wall thickness as well. The temperature gradient across the thruster wall correlates with the thruster wall thickness (the outside temperature remains cooler for a longer period for an increased thickness leading to an increased radial temperature difference across the thruster wall) and therefore also the heat flux. This in turns is directly linked to the thermal energy transported into the thruster material. Increasing the thruster wall thickness hence leads to larger amounts of thermal energy transported to the thruster wall (and therefore higher heat losses). At the same time, the thruster wall remains cooler on average, as has been proven in the underlying study. According to the Stefan-Boltzmann equation for radiating bodies (see Eq. 13 with ε being the emissivity of the material) cooler temperatures mean lower heat fluxes and are therefore associated with a longer thruster cooling duration.

$$\dot{q}_{rad} = 5.67 \cdot 10^{-8} \cdot \varepsilon \cdot T_{wall}^4 \qquad \text{Eq. 13}$$

Both effects contribute to increased cool down

periods. From an operational point of view, it is important, that the thruster cooling phase does not exceed the time between two consecutive thrust events to prevent stepwise increase of the thruster wall temperature during the de-orbit cycle consisting of approximately 400 subsequent thrust events.

Table 4: Cooling Time after Thrust Event depending on Wall Thickness and Heat Transfer Correlation.

Wall Thickness	Sinyarev	Polifke
$2.0mm$	$2115s$	$2018s$
$2.5mm$	$2539s$	$2450s$
$3.0mm$	$2935s$	$2772s$
$3.5mm$	$3303s$	$3042s$
$4.0mm$	$3639s$	$3262s$
$4.5mm$	$3948s$	$3439s$

Tab. 4 shows the simulated cooling phase duration after a thrust event. The cooling phase is defined as the time period, when the highest local temperature of the thruster falls below $310K$. The temperature of $310K$ is chosen instead of the equilibrium temperature of $296K$, since the equilibrium temperature is reached infinitesimally slowly.
The maximum cooling phase duration is approximately $66min$ for the wall thickness of $4.5mm$ and the Sinyarev correlation. This is still well within the time of one orbit revolution (approximately $90min$) and therefore two consecutive thrust events. To conclude the wall thickness of $3mm$ is chosen for the thruster as it prevents the thruster material from overheating and at the same time guarantees a sufficient cooling period and minimises the sustained heat losses.

Besides the discussed aspects, the thruster mass is also influenced by the wall thickness. However, the thruster mass is in the order of $10g$ to $30g$ for the considered wall thickness range, which is only a minor fraction of the available mass budget being $2kg$ for the entire propulsion system.

7. UNCERTAINTIES AND REQUIRED TEST CAMPAIGN

During the design process, various sources for uncertainties materialise. The most prominent in this paper is the uncertainty associated with the correlation for the heat transfer coefficient. It has a significant influence on the temperature evolution and the heat losses. The heat losses are important for the fatigue behaviour and hence for the achievable burn durations. This ultimately influences the performance of the thruster in terms of I_{sp}, since longer burn durations favour higher integral specific impulse values.
Secondly the flow field in the combustion chamber is unknown up to now. Depending on the flow field, the assumption of having a circumferentially symmetric heat transfer problem might be invalid. This again affects the fatigue behaviour of the thruster. In addition, the flow field is important for the combustion efficiency and therefore the I_{sp}.
Lastly, the thruster is manufactured additively, which comes with a high surface roughness ($R_z = 50\mu m$). This is expected to have a significant influence on the boundary layer in the throat and therefore the aerodynamic efficiency. A lower aerodynamic efficiency is associated with lower thrust levels due to reduced mass flow levels.
To assess these uncertainties, a test campaign is needed. It is planned to conduct this test campaign based on a full-scale test bench.

8. CONCLUSION

In this paper, a water electrolysis propulsion system for a 3U-CubeSat conducting a de-orbiting reference mission is described.
The system consists of an electrolyser to decompose stored water into the combustible propellants hydrogen and oxygen, gas run tanks for intermediate storage of those as well as a hot gas thruster and a cold gas thruster array. The latter enables attitude control and is operated with oxygen.
In a preliminary design phase, it is found that the transient and thermal behaviour of the system are key factors to consider. This is due to the limited propellant production rate of the electrolyser, the limited storage capacity, and the close-to-stoichiometric operation of the main thruster.
By coupling a parameterised transient simulation of the thrust event with a subsequent optimisation, a presumably optimal design point under the objective of minimising overall mass is found. Blow-down operation at moderate pressure levels of max. $15bar$ at a nominal thrust of $0.5N$ yield an I_{sp} of $\sim 300s$ with a burn time of $2.65s$. The main losses of the simulated design are attributed to ignition delay and heat flux to the thruster material.
Main findings regarding the thermal behaviour add up to

(1) Influence of the curvature, which allows longer burn durations initially predicted by neglecting the curvature of the thrust chamber inner wall.
(2) Uncertainty regarding the heat transfer coefficient, which has a significant influence on the optimal wall thickness and heat losses
(3) The optimum wall thickness at the throat is determined to be $3mm$ (for the most conservative heat transfer coefficient correlation), which results from the trade-off between overheating prevention and a minimum required cooling phase.

9. REFERENCES

[1] "Nanosatellite Database," [Online]. Available: www.nanosats.eu. [Accessed 01 04 2022].

[2] "CubeSat Design Specification Rev.14 Draft," California Polytechnic State Unicersity, 2020.

[3] A. Porter, M. Freedman, R. Grist, C. Wesson and M. Hanson, "Flight Qualification of a Water Electrolysis Propulsion System," in *Small Satellite Conference*, 2021.

[4] N. Suhadis, "Statistical Overview of CubeSat Mission," in *Proceedings of International Conference of Aerospace and Mechanical Engineering 2019*, 2020.

[5] M. Sterner and I. Stadler, Energiespeicher - Bedarf, Technologien, Integration, Springer Vieweg, 2017.

[6] N. Fernandes, A. Herbertz, B. Buergler, U. Gotzig, M. Peukert, M. Lau, J. Farnes and T. Moreira, "ELECTROLYSIS BASED WATER PROPULSION FOR FUTURE 1-TON CLASS LEO MISSION SATELLITES," in *Space Propulsion Conference*, 2020.

[7] A. Herbertz, "Theoretical Performance and Application Cases of Water Electrolysis Propulsion," *Trans. JSASS Aerospace Tech. Japan*, vol. 19, no. 2, pp. 199-204, 2021.

[8] NASA, "Spacecraft mass expulsion torques," 12 1969. [Online]. Available: https://ntrs.nasa.gov/api/citations/19700027536/downloads/19700027536.pdf. [Accessed 28 03 2022].

[9] R. W. Humble, "Space Propulsion Analysis and Design," 1995.

[10] G. Zhang, Y. Song, N. Yu, X. Tong and B. Ma, "Coaxial Hydrogen/Oxygen Gas-Dynamic Resonance Ignition Technology for Rocket Repetitive Starting," in *AIAA SPACE 2007 Conference & Exposition*, 2007.

[11] "ESPSS 3.6.0 User Manual," Empresarios Agrupados, 2022.

[12] C. U. Kirchberger, "Investigation on Heat Transfer in Small Hydrocarbon Rocket Combustion Chambers," Munich, 2014.

[13] *Nicrofer 5219 Nb / VDM alloy 718 datasheet*, VDM Metals, 2020.

[14] G. P. Sutton, Rocket Propulsion Elements, 2017.

[15] VDI, VDI-Wärmeatlas, Berlin: Springer Vieweg, 2013.

[16] R. N. Abdullaev, "Density and volumetric expansion of the Inconel 718 alloy in solid and liquid states," 2019.

[17] J. Díaz-Álvarez, "Temperature measurement and numerical prediction in machining inconel 718," 2017.

[18] C. Maeding, "Improved heat transfer prediction engineering capabilities for rocket thrust chamber layout," *Progress in Propulsion Physics*, pp. 239 - 250, 2011.